

Deep Tumor Penetrating Bioparticulates Inspired Burst Intracellular Drug Release for Precision Chemo-Phototherapy

Ruoning Wang, Yue Han, Bo Sun, Ziqiang Zhao, Yaw Opoku-Damoah, Hao Cheng, Huaqing Zhang, Jianping Zhou,* and Yang Ding*

The relevance of personalized medicine has inspired research for individually concerted diagnosis and therapy. Numerous efforts are devoted to designing drug particulates with capabilities of tumor penetrating and subcellular trafficking to concurrently discharge theranostics in response to multi-stimulations. In this study, a bioinspired particulate, formulated with whole components of native high-density lipoproteins (HDLs) and decorated with the tumor-penetrating peptide iRGD, is proposed to promote tumor penetration of HDLs (pHDLs) together with payloads. Specifically, paclitaxel (PTX), and the NIR fluorescent probe indocyanine green (ICG) are integrated into pHDLs (pHDL/PTX-ICG) for synergetic chemo-phototherapy. Inspired by lipoproteins, pHDLs are not only restored from naturally occurring materials but also possessed artificially endowed functions, leading to an enhanced cellular uptake, higher accumulation, and deep penetration into tumors without causing appreciable adverse effects, compared to reconstituted HDLs or lipid-based nanoparticles. After intravenous administration, pHDL/PTX-ICG performs a burst of intracellular drug release and imaging-guided precision chemo-phototherapy upon NIR irradiation that completely eradicates xenograft tumors. Neither recurrence nor significant toxicity is observed due to maneuvered regional photodynamic and photothermal therapy. Taken together, pHDL/PTX-ICG is proven to be a promising platform to achieve deep tumor penetration and imaging-guided chemo-phototherapy.

1. Introduction

Personalized medicine (PM) focuses on tailoring medical treatment to the characters and preferences of individual patients during all phases of healthcare from diagnosis to treatment to prognosis. Meanwhile, theranostics are an integrated form of diagnostics and medical therapy aiming to enhance the efficacy and safety of therapeutic regimes, which is paving the way toward the goal of PM and maximizing the benefits of patients.

Emerging nanotechnology has provided great opportunities with designing and generating such nanoparticle-based theranostic agents, and numerous nanosystems have already demonstrated their potential to realize enhanced therapeutic efficiency, reduced side effects, extended circulation time, and on-demand drug release.^[1] Due to tremendous focus on nanoparticles as drug delivery carriers for both contrast media and therapeutics, various synthetic nanopatforms have been designed, including polymer particles, such as poly lactic-co-glycolic acid, polymer-lipid hybrid nanoparticles,^[2] dendrimers,^[3] and graphene,^[4] among others. The development of functionalized nanoparticles was mainly encumbered by unanticipated properties and biological barriers,^[5] which would hinder the performance of nanoparticles in sophisticated physiological environments.^[6] These concerns have inspired the development of natural particulates as drug delivery vehicles, since they would seem to be nonimmunogenic, biodegradable, and biocompatible.^[7]

Viruses, pathogens, mammalian cells, and more recently, lipoproteins, have been considered as natural nanoparticle candidates for drug delivery.^[8] Among these platforms, high-density lipoproteins (HDLs) have been the focus of a great deal of research.^[9] HDL particulates are endogenous, capable of delivering various payloads (drugs, nucleic acids, and contrast media), while naturally accumulating at an endogenous target scavenger receptor-type BI (SR-BI) by apolipoprotein A-I (apoA-I). Furthermore, HDLs share a long circulation half-life due to their surface properties and particle size, which enable versatile modification.^[10]

Dr. R. N. Wang, Y. Han, Z. Q. Zhao, Dr. Y. Opoku-Damoah, H. Cheng, Dr. H. Q. Zhang, Prof. J. P. Zhou, Prof. Y. Ding
State Key Laboratory of Natural Medicines
Department of Pharmaceutics
China Pharmaceutical University
24 Tongjiaxiang, Nanjing 210009, China
E-mail: zhoujianp60@163.com; dydszyzf@163.com

Dr. B. Sun
The Center for Nanomedicine
Johns Hopkins University School of Medicine
Baltimore, MD 21231, USA

Dr. B. Sun
Department of Ophthalmology
Johns Hopkins University School of Medicine
Baltimore, MD 21231, USA

 The ORCID identification number(s) for the author(s) of this article can be found under <https://doi.org/10.1002/sml.201703110>.

DOI: 10.1002/sml.201703110

Structurally, HDL-based nanoparticulates are usually reconstituted with exogenous lipid materials and apolipoproteins, either biological or from synthetic sources. For example, synthetic HDL (sHDL) assembled by exogenous materials (including lipids and apolipoproteins) has been developed as a nanodisk-based platform for neoantigen vaccination, thereby averting potential autoimmunity triggers,^[11] while other studies have indicated that reconstituted HDL (rHDL) or sHDL might potentiate the risks of endogenous protein instability and cholesterol homeostasis confusion.^[12] Moreover, these formulations have limitations in clinical applications, such as importing immune disorders and batch variation of synthetic lipoproteins.^[13] In our previous studies, a novel green “disassembly–reassembly strategy” approach has been proposed for restoring HDLs with whole endogenous components.^[14] Instead of reconstructing HDLs with genetically engineered apolipoproteins and commercial lipids, homogeneously isolated apoA-I and dehydrated human lipids were reassembled according to their original ratio in endogenous HDLs, which are expected to recover the native structure and function, thereby minimizing any unwanted properties.

Delivering therapeutic agents into the center of the tumors is a very challenging task because of the physiological barriers segregating the core of the tumor from the blood vessels,^[15] leading to poor tumor penetration.^[16] Current targeted drug delivery carriers can only penetrate within the cell and mainly rest around the tumor vessels *in vivo* due to high interstitial pressure in the tumor and the dysfunctional structure of the tumor vessels.^[17] Of note, nanoparticles should play an important role in precisely controlling drug release in deep tumors and normal tissues. To address these challenges, receptors that are shared by vessels and cells in the tumor and related ligands with both a tumor targeting and a penetrating capacity have become leading candidates to guide the theranostic agents.^[18] Recently, the tumor-homing and tumor-penetrating cyclic peptide iRGD (CRGDK/RGPD/EC) have been demonstrated to optimize the permeability of the vascularity and tissues in a tumor-specific and receptor-dependent manner.^[19] In brief, iRGD target tumors by binding to α_v integrins first and then is cleaved to expose CRGDK/R, triggering tissue penetration with the affinity for Neuropilin-1 (Nrp-1). Thus, when nanoparticles are functionalized with iRGD, the tissue-penetrating and tissue-targeting properties would be enhanced.^[20]

Combined therapy, which targets and inhibits multiple essential pathways of tumor growth, has great potential for enhancing therapeutic efficacy and lowering drug toxicity compared to monotherapy.^[21] Paclitaxel (PTX), a naturally occurring antimetabolic chemotherapeutic (chemo) agent, showed exceptional activity for provoking cell apoptosis, while serious side effects significantly limit its clinical application.^[22] One of the strategies for decreasing the side effects of chemotherapy is to reduce the drug dose by cooperating with other treatment modalities.^[23] Indocyanine green (ICG), an NIR clinical imaging agent, has been approved by the U.S. Food and Drug Administration due to its remarkable optical features within the optimized window of *in vivo* applications.^[24] Light energy could provide ICG with bioimaging applications and produce toxic chemical species (such as singlet oxygen and hydroxyl radicals) and local hyperthermia, for the basis of photodynamic

therapy (PDT) and photothermal therapy (PTT), respectively.^[25] Moreover, various strategies were applied for the intracellular delivery of nanoparticles that have shown on-demand drug-release behaviors, which enable the release of the therapeutic agents in response to specific physical stimulus, including pH,^[26] temperature,^[27] ultrasound,^[28] magnetic field,^[29] and light.^[30] Overall, the features of light-triggered photolysis offer a more spatial and temporal control of the intracellular delivery process.

Herein, we propose a green, designed drug depot, deep tumor-penetrating HDL (pHDL), and iRGD, which was anchored on the lipid monolayer surface for drug controlled delivery. pHDL was completely reconstructed with whole components of endogenous HDLs and artificially endowed tumor penetration functions. As illustrated in **Figure 1**, hydrophobic PTX and amphiphilic ICG are simultaneously entrapped into pHDL with an improved emulsion–evaporation method. As a light-responsive and membrane-disruptive agent, ICG could realize photochemical internalization and disruption of the endo/lysosomal membrane for rapid cytoplasmic delivery and site-specific release of drug molecules to amplify antitumor therapeutic outcomes.^[31] After intravenous (*i.v.*) injection of drug-loaded pHDL particulates (pHDL/PTX-ICG), iRGD could bind to the tumor vessels, facilitate pHDL/PTX-ICG diffusion into the extra-vascular tumor parenchyma, and enable penetration into deep tumors, together with HDL-inspired natural tumor targeting for direct transmembrane delivery. Under NIR, pHDL would rapidly collapse due to Reactive oxygen species (ROS) and the hyperthermia generated by ICG, resulting in compact structure disassembly and an intracellular burst drug release. Spatially/temporally controlled drug release could be used for *in situ* fluorescence imaging and precision chemo-phototherapy at a safe level.

2. Results and Discussion

The application of green-technology-based nanomaterials for novel drug delivery design has the potential to bring about significant improvements in efficient and targeted drug delivery with biorenewability, biocompatibility, and superior binding capability. Previous research has introduced a green methodology “disassembly–reassembly strategy” to restore HDLs (rHDL), in which constitutes of HDLs were isolated, purified, and functionalized with iRGD to generate deep pHDL. The endogenous apoA-I and lipids were extracted from human plasma and obtained by the way of organic solvent/isoelectric precipitation. Figure S1 (Supporting Information) illustrates the confirmation of the extracted apolipoproteins, demonstrating clear bands of apoA-I (28.3 kDa). Moreover, apoA-I could be readily anchored to the surface of the lipid monolayer due to its amphiphilic properties to restore the original ratio of HDL, thereby providing abundant space for drug entrapment.

2.1. Synthesis and Characterization of pHDL/PTX-ICG

1,2-Distearoyl-*sn*-glycero-3-phosphoethanolamine-*N*-[maleimide (polyethylene-glycol)-2000] (DSPE-PEG₂₀₀₀-MAL) was coupled with the iRGD peptide and the DSPE-PEG-iRGD product was

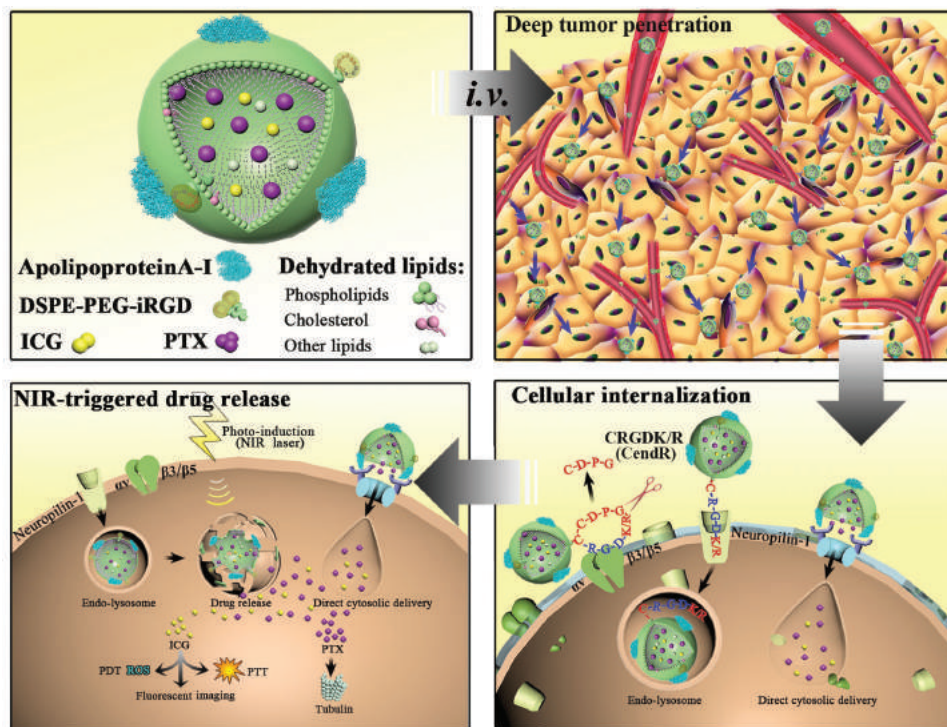


Figure 1. Schemes of pHDL/PTX-ICG and mechanism of deep tumor penetration, cellular internalization, and NIR-triggered drug release. After intravenous injection of pHDL/PTX-ICG, iRGD homes to tumors via three-step procedures: iRGD mediates binding to α_V integrins on endothelium of tumors and undergoes proteolytic cleavage to expose a binding location for Nrp-1, and then facilitates penetrating to deep tumors; meanwhile, apoA-I directs transmembrane pathway. Upon the NIR laser irradiation, intracellular burst release of drugs was triggered and the absorbed light was converted to ROS and heat generated by ICG for precision theranostics.

verified by Matrix-Assisted Laser Desorption/Ionization Time of Flight (MALDI-TOF) mass spectrometry (Figure 2A). The molecular weight (M.W.) of 4202.751 Da was in accordance with the theoretical DSPE-PEG-iRGD, which confirmed the successful synthesis. pHDL nanoparticles were formulated with DSPE-PEG-iRGD, endogenous apoA-I, and lipids through the modified emulsion–evaporation method, in which the ratio between DSPE-PEG-iRGD and HDL (w/w) was determined to be 1/8 (Table S1, Supporting Information). Hydrophobic PTX and amphiphilic ICG were simultaneously entrapped to form dual-loaded nanoparticles (pHDL/PTX-ICG). The zeta potential of rHDL/PTX-ICG was (-24.45 ± 4.12) mV, while that of pHDL/PTX-ICG showed a slight increase in the negative surface charge to (-28.45 ± 3.46) mV which accounted for iRGD presence in the corona particle (Table 1). The encapsulation efficiency (EE%) of PTX and ICG in pHDL/PTX-ICG were $(95.13 \pm 5.42)\%$ and $(50.22 \pm 8.34)\%$, respectively, demonstrating sufficient drug-loading capacity for future clinical application.

The pHDL/PTX-ICG was well dispersed in Phosphate-buffered saline (PBS) without any aggregation, and the diameter together with polydispersity index (PDI) had no dramatic changes for 60 d at 4 °C as well as in the presence of serum in Figure S3 (Supporting Information), demonstrating the controlled activity of the associated therapeutic agents (Figure 2B). The ultraviolet–visible absorption or fluorescence spectrum of the nanoparticles showed that the absorption/emission peaks of pHDL/PTX-ICG and rHDL/PTX-ICG were basically consistent with the peak of free ICG (Figure S2A,B, Supporting

Information), indicating that ICG maintained its optical properties after co-encapsulation with PTX. As shown in Figure 2C,D, PTX and ICG release from pHDL were relatively slow, $\approx 45\%$ and 49% cumulative release in the first 24 h, respectively. In comparison, cumulative PTX release from Lipos/PTX-ICG (91.40%) and rHDL/PTX-ICG (61.12%) in 24 h was much higher, and a similar trend was observed in the ICG release profile. Dual drug-loaded nanoparticles, including Lipos/PTX-ICG and rHDL/PTX-ICG, were prepared by the same methods of pHDL without apoA-I incubation or DSPE-PEG-iRGD anchoring. The sustained-release pattern of pHDL was ascribed to the controlled dissociation from the compact configuration that reassembled with whole components of the native lipoproteins. The results confirmed that pHDL should not only mimic the endogenous physiological states and behaviors but also improve the controlled release of cargo packaged in the nanoparticles when compared to Lipos, thereby leading to improved antineoplastic effects in vitro and in vivo. Afterward, pHDL/PTX-ICG was irradiated with the NIR laser to monitor the light-triggered release behavior of PTX, and $\approx 67.67\%$ of PTX was released at pH 7.4 accounting for the dissociation of pHDL after the first 6 h, whereas only 10.06% of the PTX was slowly released from the nanoparticles without irradiation (Figure 2E). Upon light irradiation, ICG can produce ROS and heat to disrupt the endo/lysosomal membrane. Meanwhile, the pHDL nanoparticles collapsed, induced the deformation of the whole core–shell structure, and accelerated drug release, which was visualized with a transmission electron microscope (TEM) shown

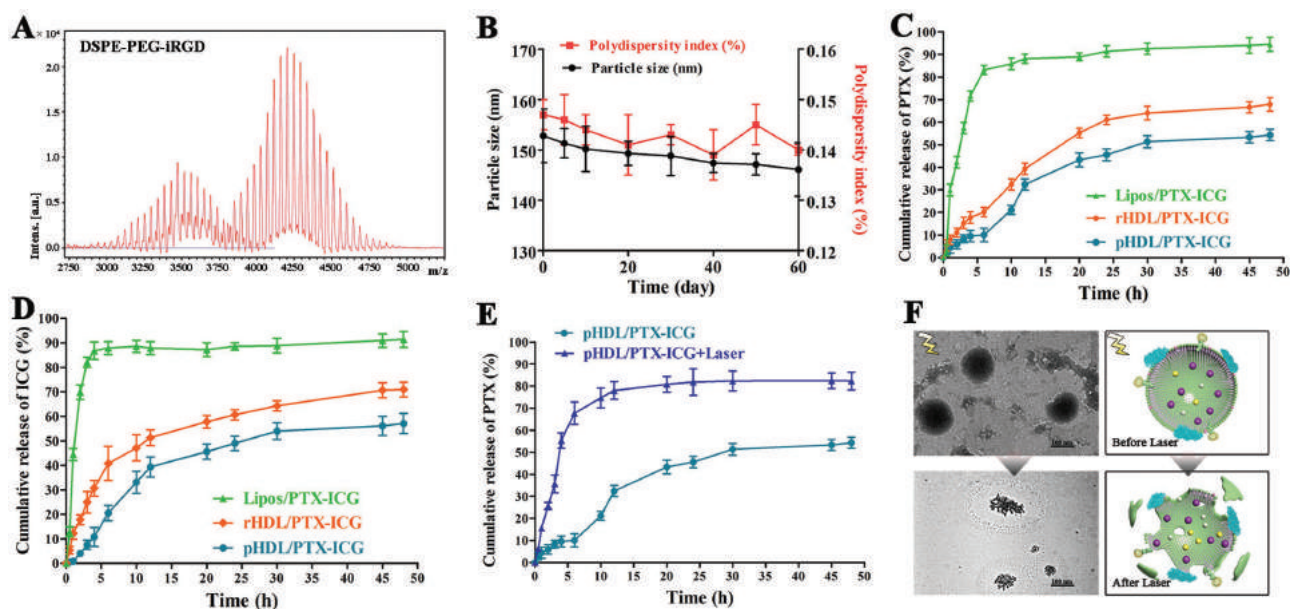


Figure 2. Synthesis and characterization of pHDL/PTX-ICG. A) MALDI-TOF-MS analysis of the conjugation of iRGD with DSPE-PEG-MAL. B) Change in diameter and polydispersity index of pHDL/PTX-ICG at 4 °C for 60 d. Release profiles of C) PTX and D) ICG from nanoparticles. E) PTX release profile from pHDL/PTX-ICG after NIR laser irradiation (808 nm, 1.2 W cm⁻²). F) TEM images of pHDL/PTX-ICG before and after NIR laser irradiation. Data are presented as mean ± SD, *n* = 3.

in Figure 2F. Collectively, the drug release burst was induced by disassembly of pHDL/PTX-ICG, which underwent the light-activated process.

2.2. Penetration and Growth Inhibition to Multicellular Tumor Spheroids

For confocal laser scanning microscopy (CLSM) imaging, remarkable fluorescence intensity enhancement of coumarin-6 (C6) and ICG was observed in the cytoplasm of the dual-labeled pHDL nanoparticles compared to the Lipos or rHDL group, indicating that pHDL could improve the cellular uptake for precision chemo-phototherapy, probably due to the high expression of integrin $\alpha_v\beta_3$ and SR-BI in A549 cells (Figures S5 and S6, Supporting Information). However, the limited penetration of anticancer agents is the culprit in the chemotherapy failure of solid tumors.^[16] Therefore, multicellular tumor spheroids were applied to monitor the penetration capacity of pHDL/PTX-ICG in the in-vivo-like tumors. As shown in Figure 3A, taking rHDL/PTX-ICG as a comparison, pHDL-mediated ICG with bright red fluorescence spread in many of the regions, indicating that pHDL/PTX-ICG (depth of 89 μ m) displayed a deeper penetration and more extensive distribution in A549

tumor spheroids than rHDL/PTX-ICG (depth of 41 μ m) did. Moreover, A549 cells in the pHDL/PTX-ICG-treated group possessed nearly fivefold higher fluorescence intensity compared with that of rHDL/PTX-ICG via analyzing the ICG fluorescence in the single cell suspension that dissociated from the spheroids using flow cytometry (Figure S7, Supporting Information). The demonstrated penetration of pHDL/PTX-ICG in tumor spheroids is the direct result of iRGD modification.

To assess the tumor growth inhibition in vitro, A549 tumor spheroids were also utilized as a model of avascular tissue for the proof of concept of the pHDL-mediated penetration chemo-phototherapy. As shown in Figure 3B, the changed ratio of the tumor spheroid volume (%) for 12 d was (168.85 ± 18.20)% in serum-free Dulbecco's modified eagle medium (DMEM), while that of the laser plus the other formulations (Lipos/PTX-ICG, rHDL/PTX-ICG, and pHDL/PTX-ICG) were (45.64 ± 9.73)%, (35.37 ± 10.25)%, and (0.66 ± 0.21)%, respectively. For microscopic observation, A549 tumor spheroids treated with pHDL/PTX-ICG+Laser were distorted and shrunk due to the cells that dissociated from the spheroid or ultimately lost 3D structure, whereas those treated with serum-free DMEM grew faster and became more compact (Figure 3C). After treatment with Lipos/PTX-ICG+Laser or rHDL/PTX-ICG+Laser, tumor spheroids stopped growing and decreased after 12 d.

Table 1. Characterization of dual-loaded nanoparticles (data are presented as mean ± SD, *n* = 3).

Nanoparticles	Diameter [nm]	Zeta potential [mV]	PDI	EE of PTX [%]	EE of ICG [%]
Lipos/PTX-ICG	98.4 ± 10.5	-17.98 ± 2.68	0.178 ± 0.030	85.13 ± 7.41	38.74 ± 2.79
rHDL/PTX-ICG	119.7 ± 5.9	-24.45 ± 4.12	0.124 ± 0.017	92.13 ± 8.71	47.44 ± 6.92
pHDL/PTX-ICG	136.2 ± 6.3	-28.45 ± 3.46	0.116 ± 0.023	95.13 ± 5.42	50.22 ± 8.34

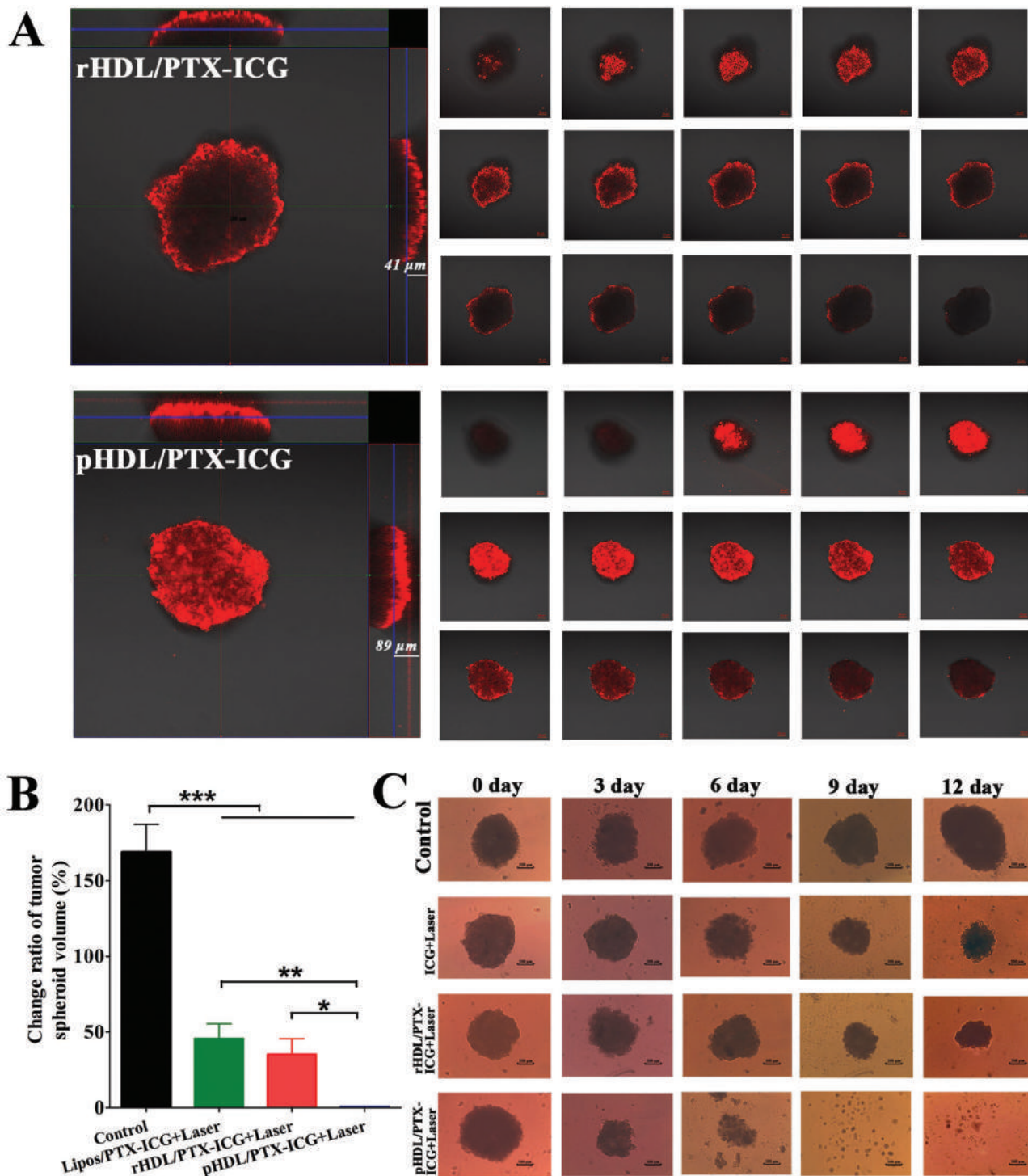


Figure 3. A) In vitro ICG penetration into A549 tumor spheroids after treated with rHDL/PTX-ICG and pHDL/PTX-ICG for 4 h. Z-stack images via CLSM were captured from top to equatorial plane of tumor spheroids in 15 μm thickness. Scale bar is 100 μm . B) The microscopic images of tumor spheroids treated with laser irradiation plus distinct formulations (Lipos/PTX-ICG, rHDL/PTX-ICG, and pHDL/PTX-ICG) and the control group on days 0, 3, 6, 9, and 12 under an inverted microscope. Change ratios of A549 tumor spheroids volume (%) after applying various formulations and nontreated control was shown on the left. * $p < 0.05$, ** $p < 0.01$, *** $p < 0.001$.

These results indicated that iRGD anchoring on the surface of pHDL nanoparticles significantly enhanced drug penetration into A549 tumor spheroids, which resulted in more efficient

delivery by PTX and ICG. pHDL could not only enhance tumor penetration but also facilitate cellular internalization within 3D spheroids. Additionally, these data provided initial evidence that

pHDL could be used to achieve chemo-phototherapy, a prerequisite for the success of the *in vivo* antitumor efficacy.

2.3. In Vitro Synergistic Chemo-Phototherapy

To investigate the combined effects of co-delivered chemotherapeutic PTX and the photosensitizer ICG, the cytotoxicity of various formulations was evaluated against A549 cells. In the absence of PTX and ICG, blank pHDL demonstrated biocompatibility with no evident cytotoxicity (Figure S8, Supporting Information). The proposed synergistic treatment modality in various drug formulations demonstrated entirely reduced cell viability without laser irradiation at 24 h (Figure 4A) and 48 h (Figure 4B), or with laser irradiation at 24 h (Figure 4C) and 48 h (Figure 4D). The cell viability of monotherapy (without laser) only slightly decreased, while the half maximal inhibitory concentration (IC_{50}) of PTX in the Lipos group within 48 h was $\approx 10.66 \mu\text{g mL}^{-1}$, which is 38.48 times more than that of the pHDL group (Table 2). This finding might be ascribed to the dual-targeting efficacy of apoA-I and iRGD-anchored nanoparticles. A549 cells treated with Taxol+Free, ICG+Laser, Lipos/PTX-ICG+Laser, or rHDL/PTX-ICG+Laser made the IC_{50} of PTX increase 90.33-, 187.33-, and 22.67-fold, respectively, compared to that of the pHDL/PTX-ICG+Laser group at 48 h, and the cell viability was significantly reduced, with gradually increased amounts of pHDL/PTX-ICG. Upon NIR irradiation, pHDL/PTX-ICG could produce ROS and hyperthermia to disrupt the endo/lysosomal or nanoparticle lipid layers and could accelerate the intracellular drug release for programmed cell apoptosis. *In vitro* triple-therapy (chemotherapy, PDT, and PTT) groups displayed a remarkable synergistic effect compared to the monotherapy groups, indicating that pHDL/PTX-ICG coupled with laser irradiation could achieve improved potency among the others through the combination of stimuli-responsive chemo-phototherapy.

To achieve single chemo, PDT, or PTT treatment efficacy, pHDL/PTX-ICG-incubated A549 cells were served without laser, with $100 \times 10^{-3} \text{ M NaN}_3$ solely, or were maintained at a constant temperature (25 °C), labeled with propidium iodide (PI) and Annexin-FITC, and further analyzed with flow cytometry. NaN_3 was used as a well-known $^1\text{O}_2$ scavenger that can annihilate singlet oxygen during laser irradiation. Chemo&PDT&PTT treatments significantly induced 72.77% of cell apoptosis/necrosis, compared with 60.74% of single chemo, 51.14% of PDT, or 42.54% of PTT (Figure 4E). The PDT group might contribute to the abundant $^1\text{O}_2$ generated by pHDL/PTX-ICG-treated cells under laser irradiation, while the decreased cell viability with increasing temperature accounts for PTT. Notably, pHDL/PTX-ICG coupled with laser irradiation (triple therapy) demonstrated much higher cytotoxicity among the groups, further confirming that NIR-triggered burst drug release contributed to enhanced therapeutic efficacy. For assessment of dual-targeting chemo-phototherapy, pHDL/PTX-ICG-mediated triple therapy has verified the optimal apoptotic efficacy with the highest total apoptotic ratio compared with the other samples (Figure S8, Supporting Information). To prove the existence of the synergistic effect of co-delivered PTX and ICG in pHDL, the combination index was determined by Chou–Talalay isobologram

formula (Figure S10, Supporting Information), which showed that the combination of PTX and ICG activity in pHDL was synergistic.

2.4. Mechanisms for Phototherapy In Vitro and In Vivo

Previous studies confirmed that the cytotoxicity of ICG under laser irradiation was triggered by different possible PTT and PDT mechanisms to facilitate cell apoptosis and necrosis. To investigate the capability of signaling modules to induce ROS generation in A549 cells, nonfluorescent 2', 7'-dichlorofluorescein-diacetate (DCFH-DA) was selected as an ROS indicator. DCFH-DA would be hydrolyzed to 2', 7'-dichlorofluorescein (DCF) and produce green fluorescence in the presence of intracellular ROS after entering cells, which can be detected at $\text{Ex} = 499 \text{ nm}/\text{Em} = 530 \text{ nm}$. The fluorescence intensity was proportional to the amount of ROS generated intracellularly. As shown in Figure 5A,B, the pHDL/PTX-ICG+Laser induced stronger fluorescence intensity in A549 cells when compared to that of rHDL or Lipos, demonstrating that the pHDL group significantly induced increased ROS levels, which is 8.49- and 80.84-fold higher than that of the tumor cells incubated with rHDL and the Lipos groups, respectively (Figure S11, Supporting Information). Although Lipos, rHDL, and pHDL possess the same concentration of ICG, differences in ROS generation probably account for the increased cellular internalization of ICG. HDL-inspired nanoparticles could be internalized into A549 via the SR-BI-mediated direct transmembrane pathway with the help of apoA-I, while more ICG-penetrated cells and was led by iRGD anchored on pHDL, producing higher ROS levels. Therefore, pHDL/PTX-ICG is promising in achieving a great PDT effect with efficient delivery to intracellular sites.

For the assessment of the *in situ* blood oxygen saturation (StO_2) content, laser plus rHDL/PTX-ICG and pHDL/PTX-ICG-treated mice were detected at three time points (pre-PDT, and 3 and 6 h post-PDT) to detect the shifts of tissue oxygenation status predicted by photoacoustic images. Regions of interest (ROIs) with a blue circle were identified by ultrasound imaging of the tumor tissue (Figure 5C), and the histograms in Figure 5D represented the average StO_2 values in the tumor ROI from ≈ 350 B scans per mouse. Prior to PDT, there was no statistically significant difference in the StO_2 between the rHDL and pHDL groups. With the elapsed time, we observed significantly lower StO_2 value of pHDL/PTX-ICG+Laser compared to that of rHDL/PTX-ICG+Laser in the post-PDT group. ICG that permeated into tumors reacted with oxygen in the surrounding tumor cells or tissue and produced adequate ROS, so that a favorable PDT effect was achieved, and hypoxia was the consequence, which contributed to necrocytosis and decreases in the metabolic consumption of oxygen. These results provide the evidence that StO_2 values of pre-PDT and 6 h post-PDT could be reliable for predicting the PDT treatment response after different treatments.

To evaluate the PTT efficiency of pHDL/PTX-ICG, temperature upgrades under laser irradiation *in vitro* and *in vivo* were monitored using an infrared thermal imaging camera. The

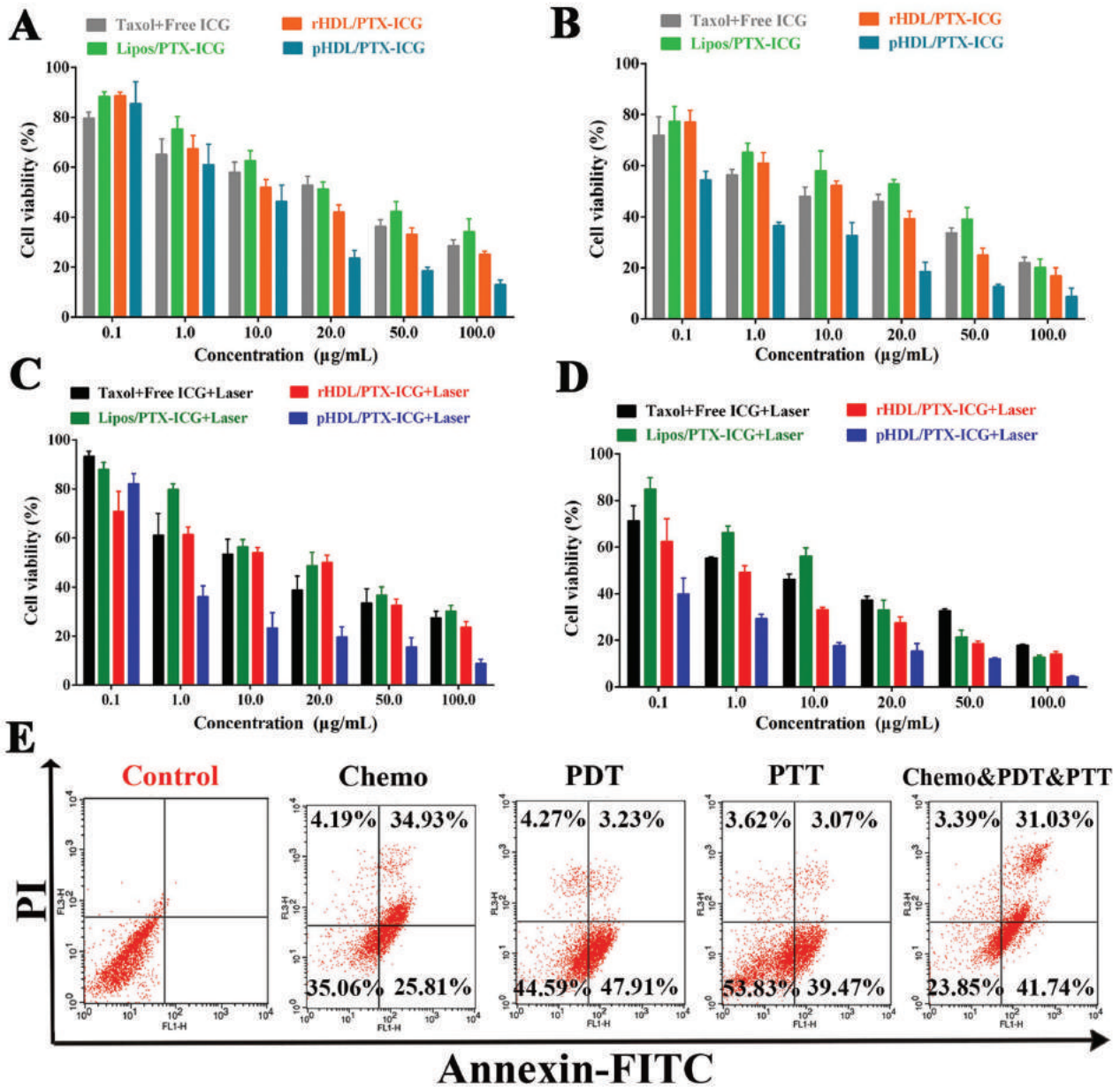


Figure 4. In vitro antitumor activity toward A549 cells. Cell viability of A549 cells treated with different nanoparticles without laser irradiation at A) 24 h and B) 48 h, or with laser irradiation at C) 24 h and D) 48 h. Data are represented as mean \pm SD, $n = 5$. E) Flow cytometry analysis of A549 cells viability following chemo, PDT, PTT, or simultaneous Chemo&PDT&PTT treatments for 6 h. Positive PI and Annexin-FITC cells were defined as apoptosis/necrotic cells. Top left quadrant: necrotic cells; top right quadrant: late apoptotic cells; bottom left quadrant: live cells; bottom right quadrant: initiation apoptotic cells.

Table 2. Inhibitory concentration (IC_{50}) of PTX in A549 cells (data are represented as mean \pm SD, $n = 5$; $***p < 0.01$, $****p < 0.001$ compared to pHDL/PTX-ICG), *means p -value.

Samples	IC_{50} [$\mu\text{g mL}^{-1}$]			
	24 h (without laser)	48 h (without laser)	24 h (with laser)	48 h (with laser)
Taxol + Free ICG	12.57 \pm 1.02***	4.04 \pm 0.47**	8.39 \pm 1.12***	2.74 \pm 0.23**
Lipos/PTX-ICG	23.44 \pm 2.13***	10.66 \pm 1.21***	16.69 \pm 2.55***	5.65 \pm 1.21***
rHDL/PTX-ICG	8.98 \pm 1.04	4.39 \pm 0.91***	6.30 \pm 0.34***	0.71 \pm 0.19**
pHDL/PTX-ICG	3.282 \pm 0.33	0.27 \pm 0.09	0.79 \pm 0.03	0.03 \pm 0.01

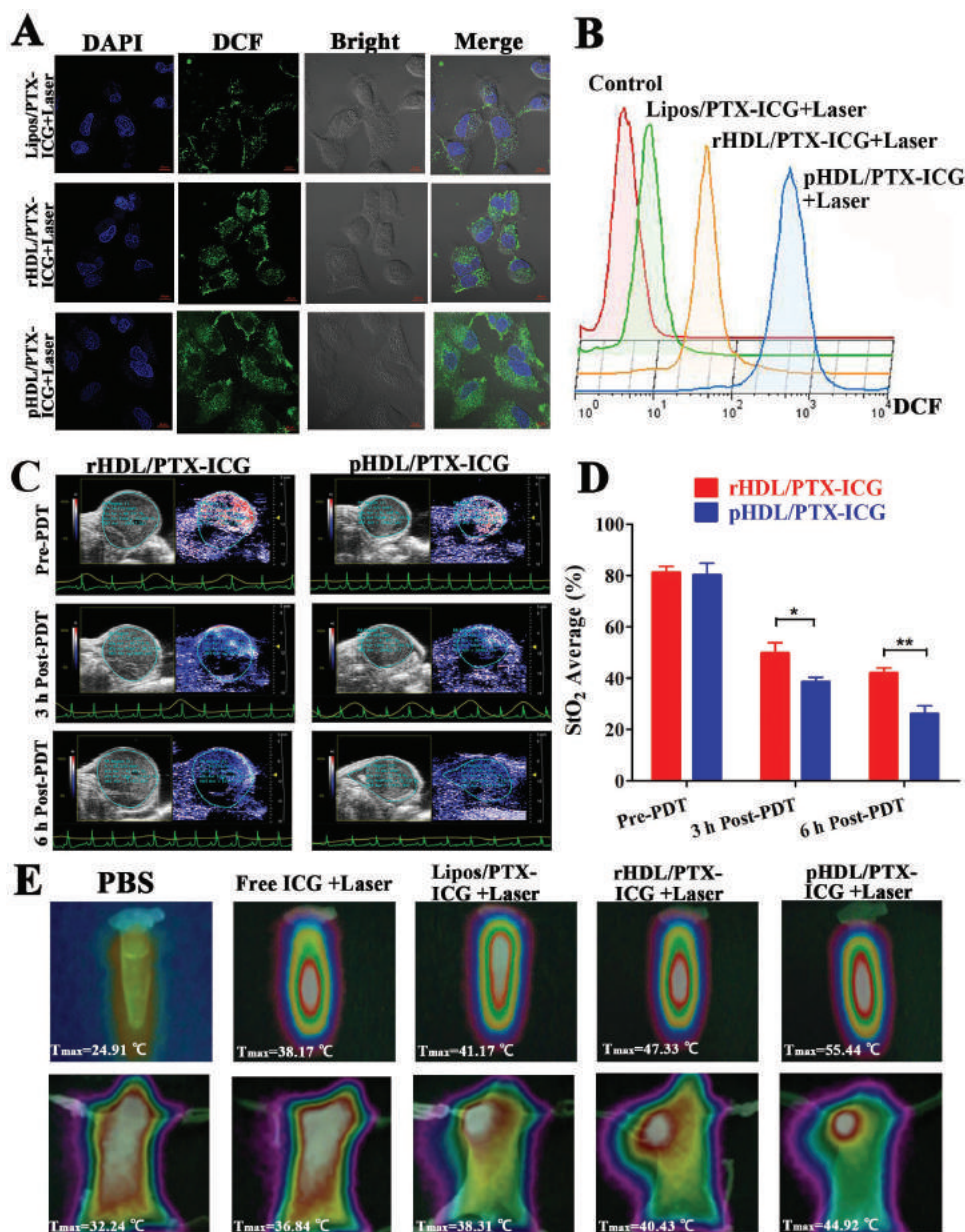


Figure 5. A) The results of intracellular ROS generation by DCFH-DA in A549 cells treated with DMEM, Lipos/PTX-ICG+Laser, rHDL/PTX-ICG+Laser, and pHDL/PTX-ICG+Laser for 4 h (blue for DAPI and green for DCF). B) Flow cytometric detection of ROS intensity in A549 cells incubated with DMEM (red), Lipos/PTX-ICG+Laser (green), rHDL/PTX-ICG+Laser (orange), and pHDL/PTX-ICG+Laser (blue) for 3 h. C) The ultrasound images in grayscale (left) and their overlaid images with oxygen saturation (StO_2) map (right); and the blue and red stand for hypoxic and oxygenated regions, respectively. D) The values of StO_2 at different time points (Pre-PDT, 3 h post-PDT, and 6 h post-PDT) for rHDL/PTX-ICG and pHDL/PTX-ICG. E) Infrared thermographic maps and maximum temperature profiles of centrifuge tubes (upper row) and A549 tumor bearing mice (lower row) treated with the free ICG, Lipos/PTX-ICG, rHDL/PTX-ICG, and pHDL/PTX-ICG exposed to 808 nm laser.

temperature of free ICG, Lipos/PTX-ICG, rHDL/PTX-ICG, and pHDL/PTX-ICG in tubes maximally increased to 38.17, 41.17, 47.33, and 55.44 °C respectively, while PBS only increased to 24.91 °C under laser irradiation (Figure 5E). ICG entrapped in nanoparticles shared higher condensed content than free ICG, and emitted thermal radiation was also captured in the nanoparticle enclosure, leading to higher energy efficiency and lower heat dissipation after laser irradiation. The increased elevated temperature of 17.27 °C produced by pHDL/PTX-ICG

would definitely cause irreversible tumor cell damage. Upon laser irradiation, the maximum temperature of tumors treated with pHDL/PTX-ICG reached 44.92 °C, leading to higher temperature response and efficient laser-dependent PTT, while the local temperature in tumors treated with free ICG only rose to 36.84 °C at most. For comparison, the Lipos and rHDL groups resulted in a temperature elevation to 38.31 and 40.43 °C. The irreversible tumor damage triggered by the temperature increase between 42 and 45 °C was attributed to hyperthermia-induced cell death

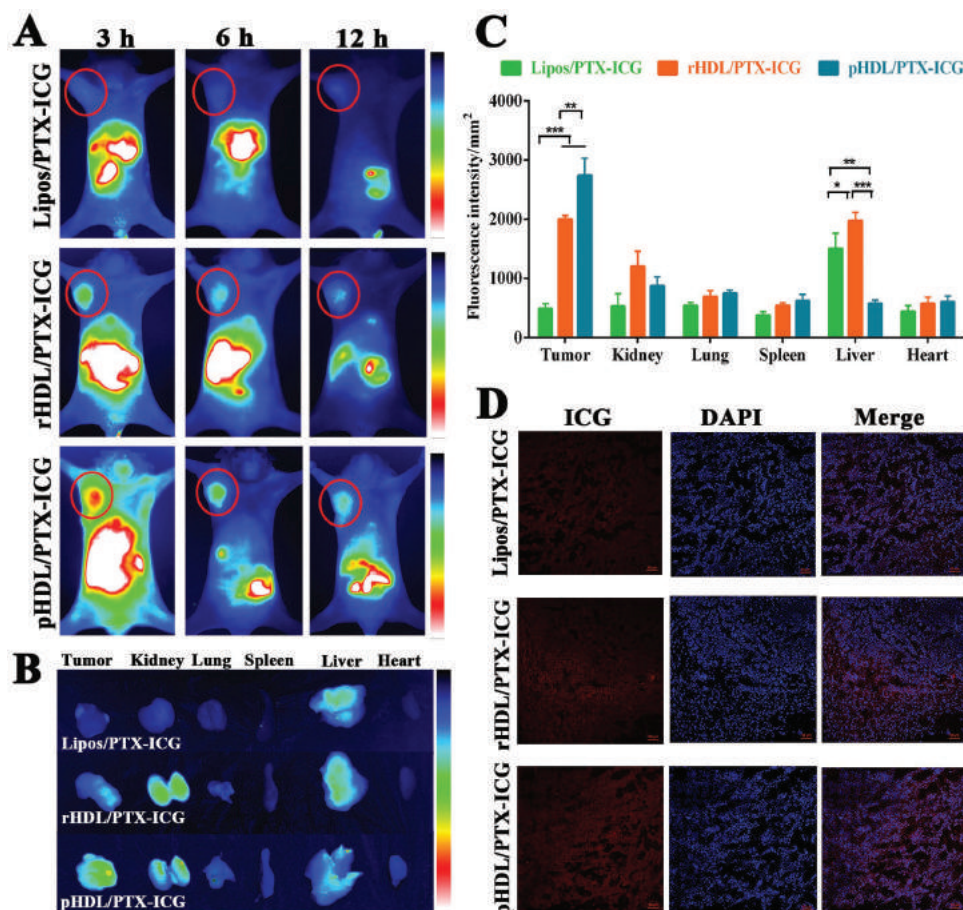


Figure 6. In vivo fluorescence (FL) imaging of nude mice bearing A549 after intravenous injection of Lipos/PTX-ICG, rHDL/PTX-ICG, and pHDL/PTX-ICG, respectively. A) In vivo FL imaging results of various formulations at various time intervals. The tumor site was marked with red circle. B) Ex vivo FL images of main normal tissues and tumors, and C) quantification of ex vivo tumor fluorescence intensity after 12 h injection (data are presented as mean \pm SD, $n = 3$; * $p < 0.05$, ** $p < 0.01$, *** $p < 0.001$). D) Confocal images of frozen tumor sections. ICG is shown in red and the nucleus in blue (DAPI). Scale bar is 50 μ m.

(PTT), including upregulation of the apoptotic gene expression levels, suppression of Tumor necrosis factor (TNF)- α resistance, mitochondrial damage, and cell coagulative necrosis.^[32] Our results indicate that pHDL/PTX-ICG possessed higher PTT efficiency among formulations, most likely because of the improved targetability and photostability of the encapsulated-ICG in the aqueous solution derived from the nanoparticles encapsulation.

2.5. In Vivo Distribution of Nanoparticles

Having confirmed that pHDL/PTX-ICG was provided with improved stability, tumor cell targeting and 3D tumor spheroid deep penetration, in vivo tumor targetability was conducted to realize the performance diagnosis. By using the intrinsic and sensitive ICG fluorescence, the signal and intensity distribution of the tumor bearing nude mice were captured at 3, 6, and 12 h after i.v. injection with a Maestro in vivo optical imaging system. As shown in **Figure 6A**, pHDL/PTX-ICG has reached tumors and achieved a prompt accumulation within 3 h, much faster than others and could remain in the tumors for up to 12 h, while most of the Lipos and rHDL were removed, suggesting

a high affinity of pHDL/PTX-ICG for the tumor parenchyma. Increased fluorescence intensity was detected in the whole liver tissue of the Lipos group 6 h after injection for lacking a tumor targeting ability, and complete Lipos clearance from the body occurred 12 h postinjection. In the meantime, much weaker fluorescence signals were visualized in tumors treated with rHDL/PTX-ICG compared with pHDL/PTX-ICG. Images of ex vivo tumor fluorescence showed much higher accumulation of pHDL compared with the rHDL group (**Figure 6B**). No obvious fluorescence signals were acquired in the heart, spleen, and lung in pHDL, while a dramatic accumulation of ICG was located in the liver of the Lipos and rHDL groups. After analysis, fluorescent intensity from the pHDL tumor was almost 1.37 times greater than that of rHDL, while that from the liver sample was lower (**Figure 6C**). These results confirmed that pHDL could specifically accumulate in the tumor site by improved targetability for in vivo diagnosis, which corresponds to the confocal images of frozen tumor sections (**Figure 6D**). Obviously, enhanced internalization of the nanoparticles and accumulation in the deep tumor region were visualized in pHDL/PTX-ICG-treated tumors compared to that of rHDL/PTX-ICG, which was attributed to targeting and penetration abilities facilitated

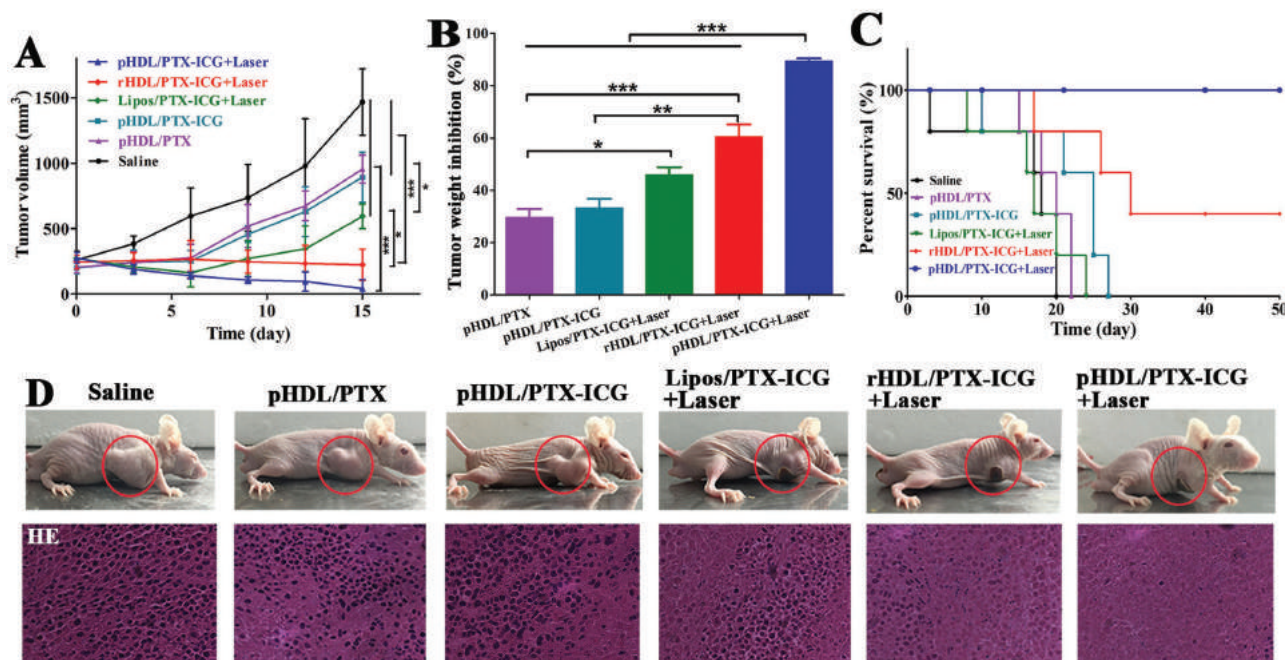


Figure 7. In vivo antitumor efficacy and pathological analysis in A549 tumor xenograft nude mice. A) Xenograft A549 tumor growth profiles in mice treated with saline, pHDL/PTX, pHDL/PTX-ICG, Lipos/PTX-ICG+Laser, rHDL/PTX-ICG+Laser, or pHDL/PTX-ICG+Laser ($n = 8$). B) Tumor weight inhibition, C) survival rates, and D) representative photographs of mice and H&E sections of tumors after treated with different formulations (data are presented as mean \pm SD; * $p < 0.05$, ** $p < 0.01$, *** $p < 0.001$).

by the iRGD peptide. Due to the overexpressed $\alpha_v\beta_3$ and Nrp-1 on the A549 tumors, the iRGD peptide could take advantage of the permeability of the tumor vasculature and cells, leading to more ICG spilled from vessels to obtain deep tumor penetration. Collectively, pHDL/PTX-ICG accumulation in tumors was able to contribute to diagnosis via sensitive molecular imaging, and then the targeted tumor could be ablated completely while sparing the surrounding normal tissues.

2.6. In Vivo Synergistic Chemo-phototherapy

To validate the merits of combination therapy, our tumor-penetrating nanoparticles were administered in A549 tumor-bearing nude mice to further evaluate the antitumor activity of pHDL in vivo. As demonstrated in **Figure 7A**, rapid tumor growth was detected in the saline group, while moderately restricted tumor growth was achieved using pHDL/PTX or pHDL/PTX-ICG and Lipos/PTX-ICG+Laser. For the rHDL/PTX-ICG+Laser-treated group, there was an 8.19% reduction in tumor volume for 15 d compared to the initial. Compared with these groups, the tumor growth was significantly inhibited in the pHDL/PTX-ICG+Laser group, achieving almost complete tumor regression. The combination of laser irradiation with Lipos/PTX-ICG, rHDL/PTX-ICG, and pHDL/PTX-ICG significantly inhibited tumor growth, of which tumor weight inhibition was 45.97%, 60.49%, and 89.41% on day 17 (**Figure 7B**). Encouragingly, pHDL/PTX-ICG+Laser led to the complete remission of tumors, leaving the original tumor site with black scars which fell off after 14 d, and no tumor recurrence was recorded in the group beyond the 50 d period. In particular, the treatment of

the pHDL/PTX-ICG+Laser, which resulted in complete remission of the tumors with all the mice surviving during the 50 d period, confirmed a satisfactory survival rate with significant elongation of the mouse life span, which was attributed to efficient cooperation of ICG-mediated phototherapy and PTX chemotherapy (**Figure 7C**). Significant tumor necrosis with severe structural damage and augmented apoptotic cells could be recorded in tumors with pHDL/PTX-ICG+Laser treatment, of which the tumors were completely ablated as shown in the representative photographs, further demonstrating the efficacy of precision chemo-phototherapy (**Figure 7D**). Notably, the introduction of tumor-penetrating iRGD peptides could improve the efficacy of chemo-phototherapy, which enhanced tissue and vascular permeability in a tumor-specific and Nrp-1-dependent manner, allowing drugs to penetrate the extra-vascular tumor tissues. Taken together, pHDL/PTX-ICG could be a multifunctional nanoparticle with integrated diagnostic and chemo-phototherapy capacity.

2.7. In Vivo Potential Side Effects of Nanoparticles

In clinical applications, most chemotherapeutic agents would induce severe side effects, such as organ toxicity and weight loss, thus compromising the therapeutic efficacy.^[17] The purposes of the synergistic combination of PTX and ICG are to overcome the undesirable side effects and toxicity due to high doses of each compound by countering the biological compensation mechanisms. Herein, safety assessments, including biochemical effects and histochemistry, were applied to evaluate whether pHDL/PTX-ICG would induce any adverse effect during the treatment,

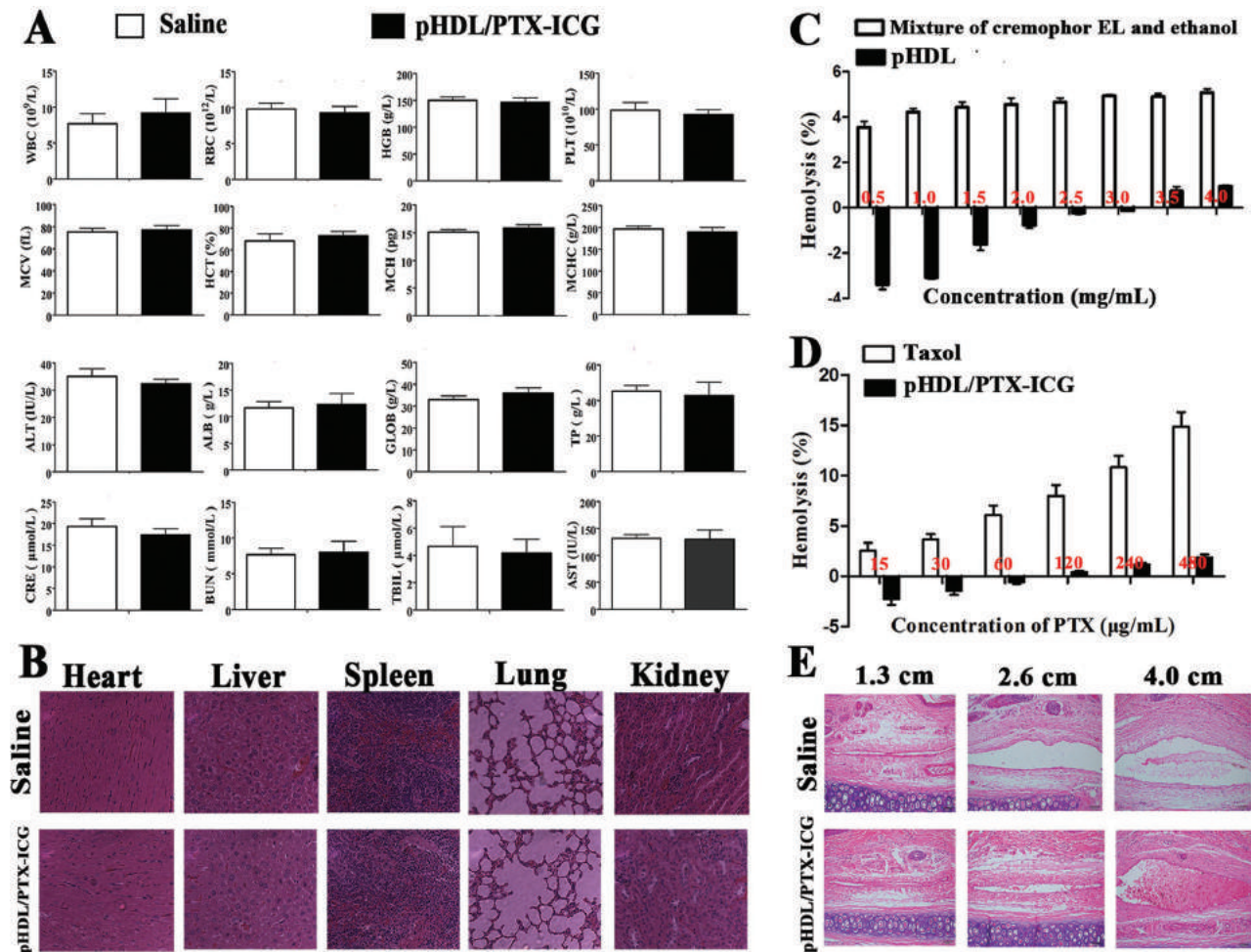


Figure 8. Safety profiles. A) Biochemical studies including hematology data (WBC, RBC, HGB, PLT, MCV, HCT, MCH, and MCHC), liver functions (ALT, ALB, GLOB, and TP), and renal functions (CRE, BUN, TBIL, and AST) in healthy nude mice treated with saline and pHDL/PTX-ICG (data are presented as mean \pm SD). B) H&E histopathological sections of tissues excised from mice in the study groups. C, D) Hemolysis assays (data are presented as mean \pm SD). E) Pathological sections of rabbit ear-rim auricular veins at or away from the site of injection. WBC: white blood cells; RBC: red blood cells; HGB: hemoglobin; PLT: platelets; MCV: mean corpuscular volume; HCT: hematocrit; MCH: mean corpuscular hemoglobin concentration; MCHC: mean corpuscular hemoglobin concentration; ALT: alanine aminotransferase; ALB: albumin; GLOB: globulin; TP: total protein; CRE: creatinine; BUN: blood urea nitrogen; TBIL: total bilirubin; and AST: aspartate aminotransferase.

where saline served as the control. As shown in **Figure 8A**, pHDL/PTX-ICG had no measurable adverse effect on the blood cells, as well as liver and renal functions throughout profiles. The peripheral blood cells, including white blood cells (WBC), red blood cells (RBC), hemoglobin (HGB), platelets (PLT), mean corpuscular volume (MCV), hematocrit (HCT), mean corpuscular hemoglobin (MCH), and mean corpuscular hemoglobin concentration (MCHC), were all within the normal range, demonstrating no syndrome, including hemolytic anemia and acute infection caused by PTX molecules. In the blood chemistry analysis, the liver function biomarkers, e.g., alanine aminotransferase (ALT), albumin (ALB), globulin (GLOB), and total protein (TP), and the renal function biomarkers e.g., creatinine (CRE), blood urea nitrogen (BUN), total bilirubin (TBIL), and aspartate aminotransferase (AST), were all normal, indicating the negligible hepatotoxicity and nephrotoxicity of pHDL/PTX-ICG. As shown in **Figure 8B**, the heart, liver, spleen, lung, and kidney were also collected for histopathological analysis, and no

pathological abnormalities, degenerations, or lesions were detected in the groups of pHDL/PTX-ICG and saline. Likewise, taking saline in comparison, no apparent signs of dehydration and other symptoms related to toxicity were recorded after pHDL/PTX-ICG injection, and there were not any noticeable behavioral abnormalities. At the tested i.v. administration dose, pHDL/PTX-ICG was relatively safe based on the results of the hematologic indicators and histopathological evaluation.

To assess the safety of the nanoparticle formulation, a hemolysis test was performed for pHDL and pHDL/PTX by taking Taxol, with a mixture of Cremophor EL and ethanol as comparisons (**Figure 8C,D**). By increasing the concentration, the mixture of Cremophor EL, ethanol, and Taxol caused significant hemolysis with 4.66% at 2.5 mg mL⁻¹ and 6.10% at 60 µg mL⁻¹, respectively. pHDL and pHDL/PTX-ICG displayed almost no hemolytic effect at the tested concentrations. Histopathological results of rabbit ear vein injected with pHDL/PTX-ICG appeared to have no apparent morphological damages,

such as thrombus or angiectasia (Figure 8E). No appreciable toxicity of pHDL/PTX-ICG was noted from the blood biochemistry, hemolysis testing, and hematological data, further corroborating that pHDL would be safe for i.v. injection.

2.8. Immunogenicity and Apolipoproteins Homoeostasis

One of primary drawbacks for nanoparticle-based drug delivery carriers is the unintended immunogenic properties, which would induce undesirable inflammatory responses or rapid clearance of particles by the immune system. The origin of immunogenicity for nanoparticles is their exogenous characteristics, i.e., the body recognizes nanoparticles as exogenous matters. To prove pHDLs are nonimmunogenic and naturally mimicking, antibody generation was measured to evaluate the immunogenic constituents of nanoparticles in vivo. For intervention (the serum collected immediately 2 d postimmunization) and withdrawal groups (the serum collected 2 weeks postimmunization), nearly no antibody generation against the apoA-I scaffold protein was observed (Figure 9A). Moreover, there is no significant difference in the content of apoA-I and apoB among saline, intervention, and withdrawal groups (Figure 9B), indicating that pHDL-mediated therapy might retain endogenous apolipoproteins stability in vivo. These data corroborated that pHDL derived from naturally occurring HDLs was fabricated with nonsignificant immunogenic

properties, inferring that pHDL is an effective and feasible vehicle with potential applications in theranostics.

3. Conclusions

In summary, we proposed a green concept to design an environmentally friendly biomaterial, pHDL, composed of endogenous apoA-I and homologous lipids, and anchoring iRGD on the lipid monolayer for deep tumor penetration. With simultaneous entrapment of PTX and ICG, pHDL showed burst release of its cargo triggered by NIR irradiation, achieving remarkable synergistic chemo-phototherapy in vitro and in vivo. We believe that pHDL/PTX-ICG introduced here can facilitate the integration of theranostic approaches that perform deep tumor penetration, intracellular burst drug release, and other possible biomedical applications, at a safe level, to exhibit great performances in diagnosis and therapy, which could pave a path to a versatile strategy for effective cancer therapy and potential clinical translation.

4. Experimental Section

Materials: The human plasma sample (precipitate IV) was donated by Tonrol Bio-Pharmaceutical Co., Ltd. (Hefei, China). Endogenous apoA-I and lipids were isolated and purified from precipitate IV utilizing an organic solvent/isoelectric precipitation method previously described with some modifications.^[14] iRGD peptide (CRGDKGPDC) was obtained from GL Bio-Chem Co, Ltd (Shanghai, China). DSPE-PEG₂₀₀₀-MAL was obtained from Avanti Polar Lipids (Alabaster, AL, USA). ICG, NaN₃, 3-(4,5-dimethylthiazol-2-yl)-2,5-diphenyltetrazolium bromide (MTT) and 4, 6-diamidino-2-phenylindole (DAPI) were purchased from Sigma-Aldrich (St. Louis, MO, USA). PTX was supplied by the Shanghai Zhongxi Pharmaceutical (Group) Co., Ltd. (Shanghai, China). Fetal bovine serum, DMEM, trypsin-Ethylenediaminetetraacetic acid (EDTA), and penicillin-streptomycin were purchased from Gibco Life Technologies (AG, Switzerland). An Annexin V-FITC/PI Apoptosis Detection Kit was obtained from Vazyme Biotech Co., Ltd (Nanjing, China). The DCFH-DA Reactive Oxygen Species Assay Kit was obtained from the Beyotime Institute of Biotechnology Co. LLC (Nantong, China). Mouse apoA-I and apoB Enzyme linked immunosorbent assay (ELISA) Kit were obtained from Shanghai Yiyuan Biological Technology Co., Ltd (Shanghai, China), and goat antimouse IgG Horse radish peroxidase (HRP)-conjugated antibody was purchased from Absin Bioscience, Inc. (Shanghai, China). All other chemicals in the study were of analytical reagent grade.

Synthesis of DSPE-PEG-iRGD: Briefly, DSPE-PEG₂₀₀₀-MAL and iRGD (1:3 w/w) were dissolved in HEPES buffer (50 × 10⁻³ M, pH 6.5), stirring for 48 h continuously. The thiol group (-SH) of iRGD is covalently bound to the maleimide group of DSPE-PEG₂₀₀₀-MAL. The reaction mixture was purified with dialysis (molecular weight cutoff: 3.5 kDa) against distilled water for 24 h, then lyophilized and stored at -20 °C for further use. The molecular weight was evaluated by MALDI-TOF mass spectrometry (Voyager Elite XL, PerSeptive Biosystems, USA).

Preparation of Nanoparticles: High-density lipoprotein-bioinspired nanoparticulates, composed of endogenous apolipoprotein A-I and lipids isolated and purified from human plasma sample (precipitate IV), were prepared as previously described with some modifications.^[14] Briefly, precipitate IV was suspended in buffer containing 65% ethanol, 1 mmol L⁻¹ EDTA and 10 mmol L⁻¹ NaHCO₃. Then, the pH value was adjusted to 7. After centrifugation, the pH of supernatant was set to 5.5, and the resulting precipitate was obtained by centrifugation. The pellet was redissolved in Tris buffer, followed by the precipitation of dehydrated lipids via the addition of an equal volume solvent mixture of ethanol and chloroform, and centrifuged. The final supernatant containing purified apoA-I, was

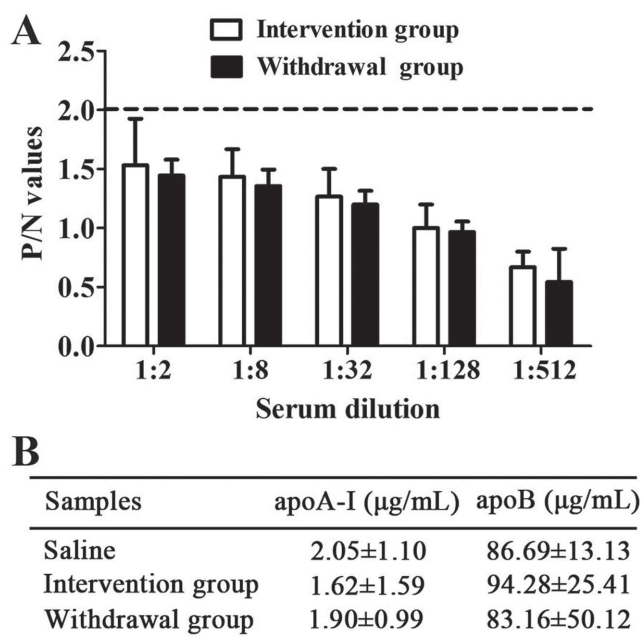


Figure 9. Assessment of immunogenicity and apolipoproteins homoeostasis of pHDL. BALB/c mice were inoculated (administered) with pHDL nanoparticles, and serum was collected 2 d (intervention group) and 2 weeks (withdrawal group) postimmunization. A) The collected serum was from each mouse in the study to obtain the curve of P/N values against serum dilution between experiment groups for assessing the immunogenicity. B) Samples were further analyzed by ELISA with the group treated with saline as a negative control for apolipoproteins homoeostasis evaluation.

concentrated by polyethylene glycol and dialyzed against phosphate buffer. Sodium dodecyl sulfate polyacrylamide gel electrophoresis (SDS-PAGE) was utilized to confirm the purified apoA-I by molecular weight.

PTX and ICG co-loaded pHDL nanoparticles (pHDL/PTX-ICG) were formulated via an emulsion–evaporation method with some modifications.^[14] Briefly, PTX and ICG (5:2 w/w) were added into the lipid solution (ethanol:chloroform = 1:1 v/v) containing DSPE-PEG-iRGD (oil phase) and mixed thoroughly. Then, the oil phase was injected dropwise into purified apoA-I solution (2 mg mL⁻¹, water phase) while being agitated at 600 rpm. Moreover, dual drug-loaded nanoparticles (Lipos/PTX-ICG and rHDL/PTX-ICG) were prepared according to the above methods without apoA-I incubation or DSPE-PEG-iRGD anchoring. The mixture stated above was sonicated at 100 W at 4 °C by utilizing a probe-type ultrasonicator (JY 92-2D, Ningbo Scientz Biotechnology Co., Ltd, Nanjing, China) for 15 min. The final suspension was transferred to the evaporator for the removal of organic solvent and then filtered via a 0.45 mm membrane. The collected samples were stored at 4 °C for further use. The same methods were introduced to prepare pHDL/PTX without ICG incorporation. Meanwhile, Taxol was prepared by dissolving 12 mg PTX in a mixture solvent of ethanol and Cremophor EL (1:1 v/v) and then sonicated for 30 min.

Cell Culture: The human lung adenocarcinoma epithelial cell line A549 was cultured in DMEM containing 10% (v/v) fetal bovine serum, 1% (v/v) penicillin, and 1% (v/v) streptomycin. Cells were cultured at 37 °C in the presence of 5% CO₂.

Characterization of Nanoparticles: To evaluate the storage stability of freshly prepared pHDL/PTX-ICG in PBS for 60 d, the diameter, zeta potential, and PDI of the samples were measured at predetermined intervals with dynamic light scattering on a Malvern Zetasizer (Nano-ZS90, Malvern Instruments, UK). The absorption spectra of the free ICG, Lipos/PTX-ICG, rHDL/PTX-ICG, and pHDL/PTX-ICG were acquired from the UV spectrophotometer. The fluorescence spectrum was obtained from a fluoro-spectro-photometer (RF-5301, Shimadzu, Japan) with an excitation wavelength at 790 nm.

To determine the encapsulation efficiency (EE%) of PTX and ICG in nanoparticles, a certain amount of drug-loaded nanoparticles was dissolved in methanol to thoroughly liberate the payloads. The amount of PTX in the nanoparticles was determined with high-performance liquid chromatography (LC-2010, Shimadzu, Japan) equipped with a UV detector and a Lichrosphre C18 column (5 mm particle size, 250 mm × 4.6 mm). The mobile phase was the mixture of methanol and water 65/35 (v/v) at a flow rate of 1.0 mL min⁻¹, and the verification method was performed as previously reported. The concentration of ICG in the diluted solution was detected by the UV spectrophotometer at 779 nm. The EE% of PTX and ICG in the nanoparticles was calculated using the equation below

$$EE\% = (\text{weight of drugs in nanoparticles} / \text{initial weight of drugs}) \times 100 \quad (1)$$

In vitro release of ICG and PTX from nanoparticles was determined by dialysis method where 1 mL of nanoparticles was loaded into a dialysis bag (molecular weight cutoff: 3.5 kDa) and incubated in 30 mL PBS (pH 7.4, containing 0.1% Tween-80) with or without an 808 nm laser at 1.2 W cm⁻² (WG1233B1 Fiber Coupled Laser System, Energylaser Opto-Electronic Technology Ltd, Beijing, China) for 5 min in a water-bath orbital shaker (100 rpm, 37 °C). At each predetermined time interval, dialysate was withdrawn and replaced with the same volume of fresh PBS. The concentration of PTX or ICG in the dialysate was detected with the method mentioned above. The freshly obtained pHDL/PTX-ICG was analyzed with TEM (JMPEG-PTMC-1230, JEOL, Japan) before and after laser irradiation.

Penetration in Avascular A549 Tumor Spheroids: Nanoparticle penetration was investigated in 3D tumor spheroid models, which were established using a liquid overlay system. In brief, agarose solution was dissolved in serum-free DMEM (2% w/w) and sterilized with an autoclave. Each well of the 96-cell culture plates coated with an agarose gel layer (100 μL), on which A549 cells (2 × 10³ in 100 μL of culture medium) were seeded. Plates were gently shaken, and tumor spheroids grew for 7 d in the presence of 5% CO₂. Afterward, tumor spheroids were treated with rHDL/PTX-ICG and pHDL/PTX-ICG (ICG of 25 μg mL⁻¹).

After incubating for 4 h, tumor spheroids were rinsed three times with PBS and then transferred to a chambered cover slip. The nanoparticles' penetration was analyzed with a confocal microscope (LSM700, Zeiss, Germany) at 639 nm (excitation wavelength of ICG). The spheroids incubated with various nanoparticles (Lipos/PTX-ICG, rHDL/PTX-ICG, and pHDL/PTX-ICG) were then treated with trypsin, and the obtained single-cell suspension was washed with PBS for flow cytometry analysis (FACS-Calibur, BD Biosciences, USA).

Growth Inhibition of Avascular A549 Tumor Spheroids: Tumor spheroids were prepared as described above. After 7 d of seeding, spheroids were incubated with DMEM containing Lipos/PTX-ICG, rHDL/PTX-ICG, and pHDL/PTX-ICG under an 808 nm laser (1.2 W cm⁻², 5 min), and those incubated with drug-free DMEM medium served as a control group. Growth inhibition was investigated by measuring the size of the tumor spheroids on days 0, 3, 6, 9, and 12 using an inverted phase microscope (ISH300, Fenyee Photoelectric Instrument and Equipment Co., Ltd, Shanghai, China) fitted with an ocular micrometer. Growth inhibition was calculated with the following equation: $V = (\pi \times d_{\max} \times d_{\min}) / 6$, where d_{\max} is the major diameter and d_{\min} is the minor diameter of each spheroid. The change ratios of the tumor spheroid volumes on the 12th day were calculated with the following equation

$$\text{Volume change ratio \%} = (V_{\text{day12}} / V_{\text{day0}}) \times 100\% \quad (2)$$

where V_{day12} is the tumor spheroid volume on 12th day after applying nanoparticles, and V_{day0} is the tumor spheroid volume prior to treatment.

In Vitro Antitumor Effect against A549 Cells: The cytotoxicity induced by nanocarriers was evaluated in A549 cells with MTT assay. A549 cells were seeded in 96-well culture plates (5 × 10³ cells per well). On achieving 70–80% confluence, cells were treated with various formulations (Taxol+Free ICG, Lipos/PTX-ICG, rHDL/PTX-ICG, and pHDL/PTX-ICG) at PTX concentrations ranging from 0.1 to 100 μg mL⁻¹ in 100 μL of serum-free medium per well. After 24 or 48 h of incubation with or without an 808 nm laser (1.2 W cm⁻², 5 min), the MTT assay was carried out, and the cell viability (%) was calculated according to a percentage relative to that of the untreated control.

Apoptosis of A549 cells was determined by the Annexin V-FITC/PI Apoptosis Detection Kit. A549 cells were seeded in 24-well plates (1 × 10⁵ cells per well), and then the cells were treated with 500 μL pHDL/PTX-ICG (ICG of 25 μg mL⁻¹) for 6 h. The chemotherapeutic effect (chemo) of pHDL/PTX-ICG on A549 cells was verified without the laser to avoid PDT/PTT effect. The PDT effect of pHDL/PTX-ICG on A549 cells was further verified by maintaining a constant temperature to avoid the PTT effect, and the PTT of pHDL/PTX-ICG was further verified by treating A549 cells with 100 × 10⁻³ M NaN₃ to avoid producing singlet oxygen during laser irradiation, while the laser spot was adjusted to cover the full area of each well. The synergistic Chemo&PDT&PTT effect of pHDL/PTX-ICG was kept under identical conditions as the experimental group. Finally, apoptosis was analyzed by using flow cytometry.

ROS Detection In Vitro: ROS generation in cells was determined by utilizing DCFH-DA Reactive Oxygen Species Assay Kit. DCFH-DA stays nonfluorescent at its reduced state, but turns into the fluorescent compound DCF after ROS generation. To qualitatively analyze ROS generation efficacy, A549 cells were seeded in confocal dishes (1 × 10⁵ cells per dish), and DCFH-DA was pretreated with cells. Following treatment with Lipos/PTX-ICG, rHDL/PTX-ICG and pHDL/PTX-ICG (ICG of 25 μg mL⁻¹), cells were irradiated under an 808 nm laser (1.2 W cm⁻², 5 min). Then, the cells were washed three times, and fluorescence images were captured by CLSM. The fluorescence of DAPI and DCF in the cells was observed with an excitation wavelength of 340 nm for DAPI and that of 488 nm for DCF. For quantitative evaluation, A549 cells were seeded in 24-well plates (1 × 10⁵ cells per well), treated with DCFH-DA and step-by-step formulations, and subsequently irradiated under an 808 nm laser. Finally, the cells were harvested and resuspended for flow cytometry analysis.

Animals and Tumor Model: BALB/c nude mice (6–7 weeks, 18–23 g) were obtained from Lingchang BioTech Co. Ltd. A549 cells (2.0 × 10⁶ cells in 50 μL PBS) were subcutaneously administered into the armpit region

and allowed to grow to a tumor size of $\approx 100 \text{ mm}^3$ (volume = length \times (width)²/2). The mice were then randomly assigned into groups. All procedures were approved by the China Pharmaceutical University Ethics Committee and carried out in accordance with the National Institute of Health Guide for the Care and Use of Laboratory Animals.

StO₂ Detection In Vivo: When the volume of A549 tumors reached $\approx 150 \text{ mm}^3$, the nude mice were injected with Lipos/PTX-ICG, rHDL/PTX-ICG, and pHDL/PTX-ICG (ICG of 1.5 mg kg^{-1}) intravenously. The photoirradiation was applied 6 h postinjection (808 nm, 1 W cm^{-2} , 5 min). Image acquisition and quantitation were carried out by the photoacoustic imaging system (Vevo LAZR, FUJIFILM VisualSonics, Inc., Canada). Mice were anesthetized and placed on a heat pad with Electrocardiogram (ECG) leads. Bubble-free, clear ultrasound gel was placed on the tumor to facilitate acoustic contact between the transducer and tumor. A linear array transducer (LZ-250, 21 MHz) was used for obtaining photoacoustic images. The average StO₂ was calculated using OxyZated and the HemoMeaZure for the Oxy-Hemo feature of the Vevo LAZR software (VevoCQ, FUJIFILM VisualSonics, Inc., Canada).

In Vivo Thermal Imaging: Nude mice bearing A549 tumors were i.v. administered saline, free ICG, Lipos/PTX-ICG, rHDL/PTX-ICG, or pHDL/PTX-ICG (ICG of 1.5 mg kg^{-1}), and the tumors were irradiated by an NIR laser (808 nm) for 5 min. Region maximum temperatures and infrared thermographic images of tumors were captured by the infrared thermal imaging camera (Ti27, Fluke, USA) and compared with those with equivalent ICG concentration in centrifuge tubes.

In Vivo Imaging and Biodistribution Analysis: To evaluate the targeting and diagnosis ability of pHDL/PTX-ICG, real-time imaging was performed by the NIR fluorescence imaging system to analyze the distribution of ICG. A549 tumor-bearing nude mice were randomly assigned into three groups, and whole-body fluorescent images were acquired at 3, 6, and 12 h after i.v. injection with Lipos/PTX-ICG, rHDL/PTX-ICG, or pHDL/PTX-ICG (ICG of 1.5 mg kg^{-1}). To further evaluate the targetability among groups, fluorescence intensity from tumors and main normal organs (heart, liver, spleen, lung, and kidneys) were detected at 12 h after injection using the ROI functions of in vivo Scion Image software. The background fluorescence observed before the injection of the nanoparticles was subtracted from the postinjection fluorescence. In addition, the cryosections of the tumor tissues (7 μm thickness) were stained with DAPI, and red fluorescence (639 nm) emitted from ICG was observed under CLSM.

In Vivo Combined Anticancer Therapy of Terminal Nanoparticles: BALB/c nude mice bearing A549 tumors were randomly assigned into six groups. When the tumor size reached $\approx 100 \text{ mm}^3$, animals were i.v. administered saline, pHDL/PTX, pHDL/ICG-PTX, Lipos/ICG-PTX+Laser, rHDL/ICG-PTX+Laser, or pHDL/ICG-PTX+Laser (PTX of 7 mg kg^{-1} and ICG of 1.5 mg kg^{-1}) every other day. For the groups treated with the laser, mice tumors were irradiated by an 808 nm laser (1 W cm^{-2} , 5 min). The tumor size and body weight were observed every other day, and the tumor weight inhibition (% TWI) was determined by the following formula

$$\text{TWI}(\%) = (\text{WC} - \text{WD}) / \text{WC} \times 100\% \quad (3)$$

of which WC and WD stand for the mean tumor weight of the control and treated groups. On day 17, three mice in each group were euthanized, and then tumors were collected and analyzed for pathological evaluation. The survival rate of the animals was calculated during the period.

Evaluations of Potential Side Effects Associated with Drug Administration: BALB/c nude mice were injected with saline via the tail vein and with pHDL/PTX-ICG (PTX of 7 mg kg^{-1} and ICG of 1.5 mg kg^{-1}) every other day. On day 16, the mice were sacrificed, and the serum was collected for biochemical studies. Serial sections of formalin-fixed tumors as well as various organs embedded in the paraffin were treated with hematoxylin and eosin (H&E). Fresh rabbit blood cells were collected and diluted in a 5% glucose solution to prepare the erythrocyte dispersion. Different volumes of formulations were mixed with erythrocyte dispersion. Negative ($A_{0\%}$) and positive ($A_{100\%}$) controls were acquired using glucose solution and distilled water, respectively. A mixture of Cremophor

EL/ethanol (1/1 v/v), Tween-80, and blank pHDL were tested as controls. All samples were incubated at $37 \text{ }^\circ\text{C}$ for 1 h, then the UV absorbance of the supernatant was detected at 540 nm, and the hemolysis percentages were calculated with the formula

$$\text{Hemolysis}(\%) = (A_{\text{sample}} - A_{0\%}) / (A_{100\%} - A_{0\%}) \times 100 \quad (4)$$

Potential venous irritation of pHDL/PTX-ICG (6 mg kg^{-1} of PTX continued for three consecutive days) was determined in New Zealand rabbits, while saline was taken as the negative control. The rabbits were euthanized 24 h after the last injection, and ear samples were excised for histopathological analysis.

Immunogenicity and Apolipoproteins' Homeostasis: To determine the immunogenicity, groups, BALB/c mice were i.v. administered pHDL every day for 28 d. Serum was collected immediately 2 d (intervention group) and 2 weeks (withdrawal group) postimmunization. The sera were collected from mice in the experimental groups and analyzed by ELISA. Immulon 2 HB microtiter plates (Thermo Fisher Scientific, Inc., Shanghai, China) were coated with the proper antigen (apoA-I of $10 \mu\text{g}$ per well) then incubated at $37 \text{ }^\circ\text{C}$ with serum at increasing dilutions for 30 min. Following incubation, the serum was removed and each well was rinsed with washing solution three times. Goat antimouse IgG HRP-conjugated antibody was added for another 30 min incubation. The bound HRP was detected by incubation with 3,3',5,5'-Tetramethylbenzidine (TMB), prior to quenching after 10 min with 1 M HCl . The reaction product was detected at 450 nm spectrophotometry, and the values were corrected by the background detected from wells that received diluent to replace the serum. The ratio of absorbance in pHDL/PTX-ICG and negative control (P/N) were calculated. If the ratio of P/N ≥ 2.0 , the result was taken as positive. Furthermore, the ELISA Kit was utilized to quantify the apolipoprotein content, including apoA-I and apoB obtained from serum.

Statistical Analysis: Results were presented as the mean \pm standard error. The differences among the groups were analyzed using one-way analysis of variance (ANOVA) analysis followed by Tukey's post-test, which were considered as to have significant differences ($*p < 0.05$, $**p < 0.01$, and $***p < 0.001$).

Supporting Information

Supporting Information is available from the Wiley Online Library or from the author.

Acknowledgements

The authors gratefully acknowledge the financial support from the National Key Research and Development Program (2017YFD0501403), and the National Natural Science Foundation of China (Grant Nos. 81501582 and 81573379). This study was also supported by the Natural Science Foundation of Jiangsu Province (Grant No. BK20171390), Graduate Cultivation Innovative Project of Jiangsu Province (Grant No. KYLX16_1179), Development Funds for Priority Academic Programs in Jiangsu Higher Education Institutions, and Fostering Plan of University Scientific and Technology Innovation Team of Jiangsu Qing Lan Project (2014).

Conflict of Interest

The authors declare no conflict of interest.

Keywords

burst intracellular drug release, deep tumor penetration, diagnosis, high-density lipoproteins, photodynamic and photothermal therapy

Received: September 8, 2017

Revised: October 19, 2017

Published online:

- [1] J. Tian, L. Ding, H. Ju, Y. Yang, X. Li, Z. Shen, Z. Zhu, J. S. Yu, C. J. Yang, *Angew. Chem.* **2014**, 126, 9698; *Angew. Chem., Int. Ed. Engl.* **2014**, 53, 9544.
- [2] M. Zheng, C. Yue, Y. Ma, P. Gong, P. Zhao, C. Zheng, Z. Sheng, P. Zhang, Z. Wang, L. Cai, *ACS Nano* **2013**, 7, 2056.
- [3] B. S. Lee, T. Amano, H. Q. Wang, J. L. Pantoja, C. W. Yoon, C. J. Hanson, R. Amatya, A. Yen, K. L. Black, J. S. Yu, *ACS Nano* **2013**, 7, 3061.
- [4] S. Kanakia, J. Toussaint, D. M. Hoang, S. Mullick Chowdhury, S. Lee, K. R. Shroyer, W. Moore, Y. Z. Wadghiri, B. Sitharaman, *Sci. Rep.* **2015**, 5, 17182.
- [5] S. A. McCarthy, G. L. Davies, Y. K. Gun'ko, *Nat. Protoc.* **2012**, 7, 1677.
- [6] J. W. Yoo, D. J. Irvine, D. E. Discher, S. Mitragotri, *Nat. Rev. Drug Discovery* **2011**, 10, 521.
- [7] H. Wang, P. Agarwal, S. Zhao, J. Yu, X. Lu, X. He, *Nat. Commun.* **2015**, 6, 10081.
- [8] C. M. Hu, R. H. Fang, K. C. Wang, B. T. Luk, S. Thamphiwatana, D. Dehaini, P. Nguyen, P. Angsantikul, C. H. Wen, A. V. Kroll, C. Carpenter, M. Ramesh, V. Qu, S. H. Patel, J. Zhu, W. Shi, F. M. Hofman, T. C. Chen, W. Gao, K. Zhang, S. Chien, L. Zhang, *Nature* **2015**, 526, 118.
- [9] a) Q. Lin, C. S. Jin, H. Huang, L. Ding, Z. Zhang, J. Chen, G. Zheng, *Small* **2014**, 10, 3072; b) K. M. McMahon, M. P. Plebanek, C. S. Thaxton, *Adv. Funct. Mater.* **2016**, 26, 7824; c) Z. Zhang, W. Cao, H. Jin, J. F. Lovell, M. Yang, L. Ding, J. Chen, I. Corbin, Q. Luo, G. Zheng, *Angew. Chem.* **2009**, 121, 9335; *Angew. Chem., Int. Ed. Engl.* **2009**, 48, 9171; d) R. Kuai, D. Li, Y. E. Chen, J. J. Moon, A. Schwendeman, *ACS Nano* **2016**, 10, 3015.
- [10] Y. Zhao, T. Imura, L. J. Leman, L. K. Curtiss, B. E. Maryanoff, M. R. Ghadiri, *J. Am. Chem. Soc.* **2013**, 135, 13414.
- [11] R. Kuai, L. J. Ochyl, K. S. Bahjat, A. Schwendeman, J. J. Moon, *Nat. Mater.* **2017**, 16, 489.
- [12] B. Zhang, X. Sun, H. Mei, Y. Wang, Z. Liao, J. Chen, Q. Zhang, Y. Hu, Z. Pang, X. Jiang, *Biomaterials* **2013**, 34, 9171.
- [13] K. I. Ansari, S. Kasiri, I. Hussain, S. A. Bobzean, L. I. Perrotti, S. S. Mandal, *Mol. Endocrinol.* **2013**, 27, 92.
- [14] R. Wang, X. Gu, J. Zhou, L. Shen, L. Yin, P. Hua, Y. Ding, *J. Controlled Release* **2016**, 235, 134.
- [15] Y. L. Su, J. H. Fang, C. Y. Liao, C. T. Lin, Y. T. Li, S. H. Hu, *Theranostics* **2015**, 5, 1233.
- [16] T. Wei, J. Liu, H. Ma, Q. Cheng, Y. Huang, J. Zhao, S. Huo, X. Xue, Z. Liang, X. J. Liang, *Nano Lett.* **2013**, 13, 2528.
- [17] C. G. Palivan, R. Goers, A. Najer, X. Zhang, A. Car, W. Meier, *Chem. Soc. Rev.* **2016**, 45, 377.
- [18] C. Song, Y. Zhang, C. Li, G. Chen, X. Kang, Q. Wang, *Adv. Funct. Mater.* **2016**, 26, 4192.
- [19] K. N. Sugahara, T. Teesalu, P. P. Karmali, V. R. Kotamraju, L. Agemy, O. M. Girard, D. Hanahan, R. F. Mattrey, E. Ruoslahti, *Cancer Cell* **2009**, 16, 510.
- [20] T. Teesalu, K. N. Sugahara, V. R. Kotamraju, E. Ruoslahti, *Proc. Natl. Acad. Sci. USA* **2009**, 106, 16157.
- [21] S. Su, Y. Tian, Y. Li, Y. Ding, T. Ji, M. Wu, Y. Wu, G. Nie, *ACS Nano* **2015**, 9, 1367.
- [22] M. E. Wall, *Med. Res. Rev.* **1998**, 18, 299.
- [23] A. Topete, M. Alatorre-Meda, P. Iglesias, E. M. Villar-Alvarez, S. Barbosa, J. A. Costoya, P. Taboada, V. Mosquera, *ACS Nano* **2014**, 8, 2725.
- [24] L. Cai, Z. Sheng, D. Hu, M. Xue, M. He, P. Gong, *Nano-Micro Lett.* **2013**, 5, 145.
- [25] Z. Wan, H. Mao, M. Guo, Y. Li, A. Zhu, H. Yang, H. He, J. Shen, L. Zhou, Z. Jiang, C. Ge, X. Chen, X. Yang, G. Liu, H. Chen, *Theranostics* **2014**, 4, 399.
- [26] C. Ju, R. Mo, J. Xue, L. Zhang, Z. Zhao, L. Xue, Q. Ping, C. Zhang, *Angew. Chem.* **2014**, 126, 6367; *Angew. Chem., Int. Ed. Engl.* **2014**, 53, 6253.
- [27] Y. Yong, X. Cheng, T. Bao, M. Zu, L. Yan, W. Yin, C. Ge, D. Wang, Z. Gu, Y. Zhao, *ACS Nano* **2015**, 9, 12451.
- [28] T. Fu, Y. Chen, J. Hao, X. Wang, G. Liu, Y. Li, Z. Liu, L. Cheng, *Nanoscale* **2015**, 7, 20757.
- [29] W. H. Chen, G. F. Luo, Q. Lei, F. Y. Cao, J. X. Fan, W. X. Qiu, H. Z. Jia, S. Hong, F. Fang, X. Zeng, R. X. Zhuo, X. Z. Zhang, *Biomaterials* **2016**, 76, 87.
- [30] C. Qian, J. Yu, Y. Chen, Q. Hu, X. Xiao, W. Sun, C. Wang, P. Feng, Q. D. Shen, Z. Gu, *Adv. Mater.* **2016**, 28, 3313.
- [31] T. Yin, J. Liu, Z. Zhao, Y. Zhao, L. Dong, M. Yang, J. Zhou, M. Huo, *Adv. Funct. Mater.* **2017**, 27, 1604620.
- [32] Z. Wang, S. Li, M. Zhang, Y. Ma, Y. Liu, W. Gao, J. Zhang, Y. Gu, *Adv. Sci.* **2016**, 4, 1600327.